

Automatic Active Model Initialization via Poisson Inverse Gradient

Bing Li, *Student Member, IEEE*, and Scott T. Acton, *Senior Member, IEEE*

Abstract—Active models have been widely used in image processing applications. A crucial stage that affects the ultimate active model performance is initialization. This paper proposes a novel automatic initialization approach for parametric active models in both 2-D and 3-D. The PIG initialization method exploits a novel technique that essentially estimates the external energy field from the external force field and determines the most likely initial segmentation. Examples and comparisons with two state-of-the-art automatic initialization methods are presented to illustrate the advantages of this innovation, including the ability to choose the number of active models deployed, rapid convergence, accommodation of broken edges, superior noise robustness, and segmentation accuracy.

Index Terms—Active contours, active models, active surfaces, deformable models, deformable surfaces, initialization, Poisson's equation, Poisson inverse gradient, snakes.

I. INTRODUCTION

IN the last two decades, active models [1], or *deformable models* [2], have emerged as a popular and powerful tool for image segmentation [3]–[8] and object tracking [9]–[13]. Although there are several existing versions of active models [14]–[17], the most widely used active models include *active contours* (also known as *snakes* or *deformable contours*) [1] and *active surfaces* (also known as *deformable surfaces*) [2]. The active models deform on the image domain and capture a desired feature by minimizing a model energy functional subject to certain constraints. The model energy functional usually contains two terms: a model internal energy, which constrains the smoothness and tautness of the model, and a model external energy, which attracts the elastic model to the *features of interest*.

Although extensive research has been completed to improve the active model performance [3], [18], [19], the subject of active model initialization has received considerably less attention. The initialization is a critical factor in the ultimate solu-

tion quality of the active model, because a poor initialized active model may become stuck at local energy minimum and fails to capture the features of interest. The most popular and convenient way is to initialize the active models by employing some naïve geometric model such as a circle in 2-D or sphere in 3-D. The major drawback of this simple initialization approach is that the active model may need a large number of iterations to converge or may converge to clutter away from the desired target. An alternative is manual initialization via manual selection of initial points. Even though manual initialization is effective, manually drawing a complex 3-D surface, for example, is an extremely difficult and error-prone process. Approaches have been published to simplify the manual initialization process [20]–[22], whereas other researchers proposed automatic initialization method by analyzing the external force field [23]–[26].

The main contribution of this paper is to provide a new method to automatically initialize parametric active models by estimating the underlying external energy field via solution of Poisson's equation. The proposed method selects an initial model with an associated energy that approaches the minimum energy. This novel method accelerates the active model convergence and improves the active model performance via initializing the active model close to features of interest. Our method is limited to parametric active contours [1] and discrete active surfaces [4], [27], thus the benefits of the geometric or level set implementation are precluded by this initialization.

This paper is organized as follows. We review the basics of active surfaces in Section II, and introduce a way to estimate the underlying external energy field from the external force field, *Poisson inverse gradient* (PIG), in Section III. Based on the estimated external energy field, the automatic initialization methods for single and multiple active models are detailed in Section IV. All equations are given for 3-D images, from which the analogous 2-D equations can be formulated accordingly. Several promising properties of this new initialization method are demonstrated by a set of examples and comparisons in Section V. The salient properties of PIG initialization include robustness to noise, accommodation of broken edges and multiple objects, explicit choice of the number of active models deployed, improved segmentation accuracy and rapid convergence to features of interest. Finally, we draw conclusions in Section VI.

II. BACKGROUND

A. Active Surfaces

An active surface is defined by mapping a bivariate parameter domain $(m, n) \in [0, 1]^2$ into $(x, y, z) \in \mathbb{P}_3^3$, where a surface

Manuscript received July 22, 2007; revised April 8, 2008. First published June 13, 2008; last published July 11, 2008 (projected). This work was supported in part by the National Institutes of Health EB001826, in part by CDMRP W81XWH-01-1-0240, and in part by the U.S. Army Research Office 46850-CI. The associate editor coordinating the review of this manuscript and approving it for publication was Prof. Vicent Caselles.

B. Li is with the C. L. Brown Department of Electrical and Computer Engineering, University of Virginia, Charlottesville, VA 22904 USA (e-mail: bingli@virginia.edu).

S. T. Acton is with the C. L. Brown Department of Electrical and Computer Engineering/Biomedical Engineering, University of Virginia, Charlottesville, VA 22904 USA (e-mail: acton@virginia.edu).

Color versions of one or more of the figures in this paper are available online at <http://ieeexplore.ieee.org>.

Digital Object Identifier 10.1109/TIP.2008.925375

point is given by $\mathbf{v}(m, n) = [x(m, n), y(m, n), z(m, n)]^T$. The surface is deformed by minimizing

$$\varepsilon_{\text{as}} = \int_0^1 \int_0^1 [E_{\text{int}}(\mathbf{v}) + E_{\text{ext}}(\mathbf{v})] dm dn \quad (1)$$

where $E_{\text{int}} : P_2^3 \rightarrow P_2$ denotes the internal energy that encourages a smooth surface, and $E_{\text{ext}} : P_2^3 \rightarrow P_2$ denotes the external energy, the value of which is small at the features of interest, such as edges [1], [2], [28]. A typical internal energy is defined as

$$E_{\text{int}}(\mathbf{v}) = \frac{1}{2} \left(\alpha \sum_a \left| \frac{\partial \mathbf{v}}{\partial a} \right|^2 + \beta \sum_{a,b} \left| \frac{\partial^2 \mathbf{v}}{\partial a \partial b} \right|^2 \right) \quad (2)$$

where α and β are weighting parameters constraining the degree of the smoothness and tautness of the surface, respectively.

Typical external energy formulations for a gray-level image $I(x, y, z)$ are given as [1]

$$E_{\text{ext}}^{(1)}(x, y, z) = -|\nabla I(x, y, z)|^2 \quad (3)$$

or

$$E_{\text{ext}}^{(2)}(x, y, z) = -|\nabla [G_\sigma(x, y, z) * I(x, y, z)]|^2 \quad (4)$$

where $G_\sigma(x, y, z)$ is a 3-D Gaussian function with standard deviation σ , $*$ denotes linear convolution, and ∇ denotes the gradient operator. If the image is a binary image, where the features of interest are ones and the background is zero, the typical external energies are expressed as [28]

$$E_{\text{ext}}^{(3)}(x, y, z) = -I(x, y, z) \quad (5)$$

or

$$E_{\text{ext}}^{(4)}(x, y, z) = -G_\sigma(x, y, z) * I(x, y, z). \quad (6)$$

Although a large σ may distort the features of interest, a large σ is often necessary to suppress the noise and increase the capture range of the active contours.

At the minima of (1), the surface must satisfy the Euler–Lagrange equation

$$\alpha \Delta_{\text{mn}} \mathbf{v} - \beta \Delta_{\text{mn}}^2 \mathbf{v} - \nabla E_{\text{ext}} = 0 \quad (7)$$

where $\Delta_{\text{mn}} \mathbf{v} = (\partial^2 \mathbf{v})/(\partial m^2) + (\partial^2 \mathbf{v})/(\partial n^2)$ is the surface Laplacian operator. This equation can be considered as a force balance equation

$$\mathbf{f}_{\text{int}}(\mathbf{v}) + \mathbf{f}_{\text{ext}}(\mathbf{v}) = 0 \quad (8)$$

where $\mathbf{f}_{\text{int}}(\mathbf{v}) = \alpha \Delta_{\text{mn}} \mathbf{v} - \beta \Delta_{\text{mn}}^2 \mathbf{v}$ is the internal force to constraint the smoothness and tautness of the surface, and

$$\mathbf{f}_{\text{ext}}(\mathbf{v}) = -\nabla E_{\text{ext}}(\mathbf{v}) \quad (9)$$

is the standard external force that draws the surface toward the features of interest. If the *edge map* is defined as

$$f = -E_{\text{ext}} \quad (10)$$

then $\mathbf{f}_{\text{ext}} = \nabla f$, i.e., the standard external force is the gradient of the edge map. The edge map can be calculated by various edge detectors, such as the Canny edge detector [29] and Monga–Deriche edge detector [30].

To solve (8), $\mathbf{v}(m, n)$ is treated as a function of time t . The solution is obtained when the steady state solution of the following gradient descent equation:

$$\frac{\partial \mathbf{v}(m, n, t)}{\partial t} = \mathbf{f}_{\text{int}}(\mathbf{v}(m, n, t)) + \mathbf{f}_{\text{ext}}(\mathbf{v}(m, n, t)) \quad (11)$$

is reached from an initial surface $\mathbf{v}(m, n, 0)$.

B. External Forces

A number of research groups have generalized (8) via replacing the standard external force with the sum of other forces generated from the image and/or the contour [18], [28]. In addition to the standard external force (9), a variety of external forces have been proposed to improve the performance of snakes. The external forces can be generally classified as dynamic forces and static forces [18]. The dynamic forces are those that depend on the snake and, as a result, change as the snake deforms. The static forces are those that are calculated from the image only, and remain unchanged as the snake deforms.

The *pressure force*, also known as the *inflation force*, used in balloon models is an useful dynamic force that pushes the active model either outward (inflation) or inward (deflation) [6], [27], [28], [31]. Although the pressure force can avoid spurious edges, the pressure force causes leakage problem when there are significant gaps in the edges [18]. Another limitation of the snake using a pressure force is that it must be initialized either inside or outside the targeted object.

The major drawback of standard external forces is that the force field has an initially zero magnitude in the homogeneous regions of the image. Therefore, the initial active model must be close to the features of interest in order to converge. There are several attractive candidates for the static external force with large capture range, including the *distance force*, *gradient vector flow* (GVF), and *vector field convolution* (VFC). The distance force points to the closest edge in terms of Euclidean distance by taking the negative gradient of the Euclidean distance transformation of the edge points [28]. In this case, the edge points are extracted from the edge detector, such as the Canny edge detector [29]. The GVF field is calculated as an iterative diffusion of the standard external force [18], which outperforms the distance force by providing a large capture range and the ability to capture boundary concavities. And third, the VFC field is computed by convolving the edge map f with a predefined vector field kernel [19], [32], which has superior noise robustness and lower computational cost than the GVF field.

C. Active Model Initialization

Initialization is a critical factor in the ultimate solution quality of the active model, which has not been investigated thoroughly in the literature. The most popular and convenient way to initialize active models is by employing some naïve geometric shapes, such as a rectangle in 2-D or a sphere in 3-D [8], [11], [17]–[19], [27], [33], [34]. Major drawbacks of this simple initialization approach include a large number of required iterations and convergence away from features of interest. These problems can be attributed to a poor shape approximation of features of interest. A poorly placed naïve geometric shape may never converge to the right boundary.

An effective alternative choice is manual initialization via connecting user-selected initial points. However, manually drawing a complex 3-D surface is an extremely tedious and error-prone process. In practice, an user-friendly interface is usually necessary for users to manually select points and initialize a polyhedral model for active surfaces [35], [36]. To reduce the complexity of manual initialization for active models, Neuenschwander *et al.* first proposed to initialize open active contours by only two end points in 1994 [20]. Cohen and Kimmel enhanced this approach via a minimal path method and extended it to closed active contours [21]. Most recently, Ardon and Cohen further extended this minimal path initialization approach to 3-D images for active surfaces [22]. Although these methods do simplify the manual initialization process, manual drawing is still necessary. For example, two points and two contours are needed for each active contour and each active surface, respectively. In addition, the Ardon–Cohen method is limited to a single object with a cylinder-like topology [22].

Since the introduction of the GVF external force [18], various researchers have made efforts to initialize active contours by analyzing the GVF external force field [23]–[26]. Ge and Tian proposed an automatic initialization method for multiple active contours by placing small circles at centers of divergence [23]. The *center of divergence* (CoD) in 2-D is defined as the point from which the GVF vectors of all neighboring pixels emanate. Because this method tends to initialize more than the desired number of active contours, i.e., the image is over-segmented, a region merging postprocess is needed to remove the pseudo boundaries. He *et al.* introduced a semi-automatic initialization method with a similar idea [24]. Tauber *et al.* generalized the concept of centers of divergence and proposed a quasi-automatic initialization method requiring only one user-defined point [25].

Li *et al.* introduced an automatic initialization method via segmenting the external force field [26]. By treating the quantized external force field and the binary edge map as a graph, the external force field is divided into regions by seeking weakly connected components in the graph. Each region boundary is then initialized as an active contour. This *force field segmentation* (FFS) method always initializes one active contour outside each connected component in the binary edge map. Therefore, the FFS method can not accommodate objects with broken edges or objects surrounded by extraneous edges. Although these force field analysis techniques improve active contour performance by placing the simple shape initial model at the

correct place, the initial model is still isolated from features of interest and requires a large number of iterations to converge.

In addition to the approach of forming an initialization for standard active models, more sophisticated active models may be used to improve the initialization. The segmentation results from the coarse-to-fine active models [4], the multiscale active models [37], [38], and the adaptive sampling active models [39] can be applied. The marching cubes algorithm [40] and the digital surfaces algorithm [41] are able to extract surfaces from binary 3-D images as initial surface for active surfaces. Unlike the CoD and FFS methods discussed in previous paragraphs, these methods are not designed for solely initializing standard active models.

III. POISSON INVERSE GRADIENT

Although active models deform according to the generalized force balance (11), from another point of view, it is still an energy minimization problem. The relationship between the external force field and the external energy field is analogous to the relationship between the gravity and the gravitational potential energy in physics. Recall that the external force field is defined as the negative gradient of the external energy field in (9). Then, for a given static external force field \mathbf{f} , there should exist an external energy field E such that the negative gradient of E is \mathbf{f} . Unfortunately, \mathbf{f} is not a conservative vector field in general, i.e., \mathbf{f} can not be expressed as the negative gradient of any scalar function. We must, therefore, approximate E in a meaningful way. In this section, we introduce a method to estimate the external energy field E given the static external force \mathbf{f} by solving Poisson's equation, from which the initial model is extracted.

Let Ω be a subset of P_2^3 with boundary $\partial\Omega$. Let $E: P_2^3 \rightarrow P_2$ be an unknown scalar function and $\mathbf{f}: P_2^3 \rightarrow P_2^3$ be a known vector field defined over Ω , as shown in Fig. 1. The *Poisson inverse gradient* (PIG) approach estimates the external energy field E such that the negative gradient of E is the closest vector field to \mathbf{f} in the L_2 -norm sense [42]

$$E = \arg \min_E \iint_{\Omega} |-\nabla E(x, y, z) - \mathbf{f}(x, y, z)|^2 dx dy dz \quad (12)$$

with certain boundary conditions. To solve (12), E is the unique solution of the following Poisson's equation [43]

$$\Delta E(x, y, z) = -\text{div} \mathbf{f}(x, y, z) \text{ for } (x, y, z) \in \Omega \quad (13)$$

where $\Delta = (\partial^2)/(\partial x^2) + (\partial^2)/(\partial y^2) + (\partial^2)/(\partial z^2)$ is the Laplacian operator, and

$$\text{div} \mathbf{f} = \frac{\partial u}{\partial x} + \frac{\partial v}{\partial y} + \frac{\partial w}{\partial z} \quad (14)$$

is the divergence of $\mathbf{f} = [u, v, w]$. In order to solve (13), the boundary conditions must be specified. For active models, instead of the Neumann boundary conditions [44], the Dirichlet boundary conditions [45]

$$E|_{\partial\Omega} = E_{\text{ext}}|_{\partial\Omega} = -f|_{\partial\Omega} \quad (15)$$

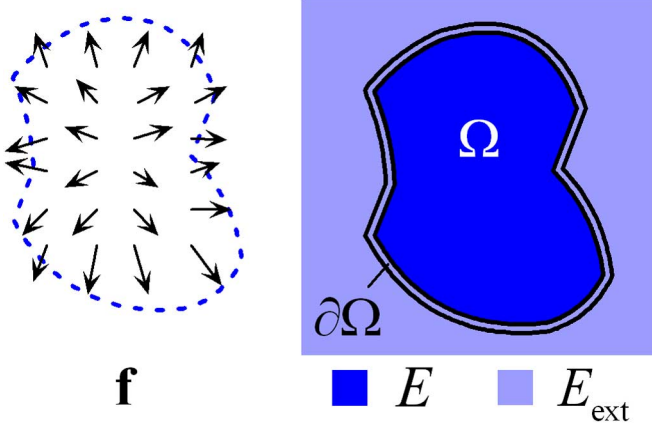


Fig. 1. Poisson inverse gradient estimates the external energy field E based on the external force field \mathbf{f} in domain Ω with boundary $\partial\Omega$.

are specified to maintain fidelity with respect to the edge map f , which is used to generate the vector field \mathbf{f} .

A. Numerical Solution

Numerical solutions to Poisson's equation with Dirichlet boundary conditions has been well studied [46]–[49]. For digital images, the problem can be discretized directly using the underlying pixel grid, and the region Ω becomes a finite set of points, denoted by ω . To be specific, on a discrete grid $[1, M_x] \times [1, M_y] \times [1, M_z]$, the discrete domain region ω is defined as a collection of finite pixels. For each pixel p in ω , let N_p denote the set of its 6-connected neighbors. The continuous boundary $\partial\Omega$ of the region Ω now becomes the discrete boundary $d\omega$, which is defined as a collection of pixels surrounding the region ω

$$d\omega = \{p \notin \omega : \omega \cap N_p \neq \emptyset\}. \quad (16)$$

Let \mathbf{f}_p denote the value of \mathbf{f} at p . The problem is then to solve the discrete Poisson's equation

$$\Delta E_p = -\text{div} \mathbf{f}_p \text{ for all } p \in \omega \quad (17)$$

with Dirichlet boundary conditions

$$E_p = -f_p \text{ for all } p \in d\omega. \quad (18)$$

Using a finite difference approximation of the Laplacian and divergence operators, (17) can be rewritten as: for all $p \in \omega$

$$\sum_{q \in N_p \cap \omega} E_q - |N_p| E_p = \sum_{q \in N_p \cap d\omega} f_q + \text{div} \mathbf{f}_p \quad (19)$$

where the number of neighbors $|N_p|$ might be fewer than 6, depending on if p is on the image border. Note that for pixels p interior to ω , i.e., all the neighbors of pixel p belong to the

TABLE I
COMPLEXITY OF DIFFERENT POISSON SOLVERS WITH N PIXELS [47]–[51]

SOR	CG	FFT	multigrid
$O(N^{1.5})$	$O(N^{1.5})$	$O(N \log N)$	$O(N)$

region ω ($N_p \subset \omega$), the boundary term on the right hand side of (19) can be ignored, thus (19) reduces to

$$\sum_{q \in N_p} E_q - |N_p| E_p = \text{div} \mathbf{f}_p. \quad (20)$$

In a linear algebraic sense, (19) defines a symmetric positive-definite banded sparse system, which can be solved in numerous ways. These solutions include successive over-relaxation (SOR) [50], conjugate gradient (CG) techniques [51], fast Fourier transform (FFT) techniques [47] and multigrid methods [48], [49]. The computational complexity comparison is shown in Table I. A complete review of discrete Poisson solvers is beyond the scope of this paper. We implemented the PIG initialization on a Dell Dimension 9150 computer with Pentium D 2.8-GHz CPU, 1-GB RAM, and MATLAB 7.0. On this platform, 0.4 s are required to solve a 20 000 pixel system. A parallel FFT-based approach [47] or a multigrid implementation [48] in C will provide a faster solution for larger regions.

B. Vector Field Visualization

PIG initialization provides a way to visualize the external force field and compare different vector fields. The external energy of any given active models defined in the image domain can be estimated based on the estimated external energy field, which can be used for comparing the quality of different initial models.

One intuitive way of vector field visualization is to set the whole image as ω with Neumann boundary conditions, and ignore the edge map f . While this approach is valid, the useful information in the edge map f is preserved if Dirichlet boundary conditions are chosen and the discrete region is defined as

$$\omega = \{p : f_p \leq \tau_f\} \quad (21)$$

where τ_f is a threshold defining edge pixels. All the pixels in the edge map f that have a value larger than τ_f are preserved as features of interest (edges) and used as boundary conditions, whereas other pixels are treated as the region ω . Morphological filters, such as the area close filter, can be employed to further refine the region ω .

As shown in Fig. 2, the GVF force field and the VFC force field are calculated from a noisy magnetic resonance (MR) image of a human ankle, which is demonstrated by streamlines. *Streamlines* are traces that exhibit where points move when placed in a force field. After thresholding the edge map using (21) and applying the area close morphological filter to eliminate small features, the region ω is shown as white pixels in Fig. 2(b). The estimated external energy fields overlapped

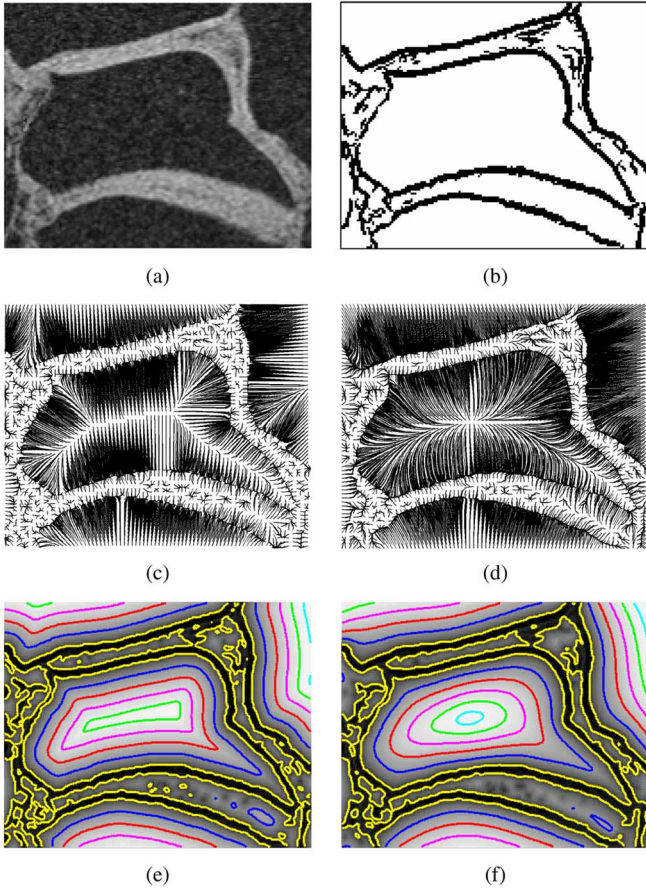


Fig. 2. (a) MR image slice of a human ankle. (b) The region Ω used for PIG initialization is shown in white. Streamlines generated from the (c) GVF and (d) VFC field. The estimated external energy of the (e) GVF and (f) VFC field, respectively, superposed with isolines.

with the isolines provide a different view of the external force fields, a.k.a., the underlying external energy, as demonstrated in Fig. 2(e) and (f). An *isoline* is a curve connecting points of equal PIG value, and this value is termed *isovalue*. Note that the streamlines should be orthogonal to the isolines, because the direction of streamlines is the gradient direction of the estimated external energy field. By observing Fig. 2, we find that the isolines close to features of interest can be used as a good initialization for active contours.

The estimated external energy field is closely related to the force field analysis methods [23]–[26]. The center of divergence corresponds to the local maxima of the estimated external energy field, and the boundaries of weakly connected components in the FFS method correspond to ridges of the estimated external energy field. The PIG solution can also be considered as a generalized distance transform, where the distance at one point is determined by the streamline length from this point to the closest edge point on the streamline.

IV. AUTOMATIC ACTIVE MODEL INITIALIZATION

After calculating the estimated external energy field from the external force, a high-quality initial active model can be achieved by selecting an isoline or isosurface with a proper isovalue. Analogous to the isolines in 2-D, *isosurfaces* in 3-D

are surfaces that pass through the isovalues of the external energy field. The marching cubes algorithm is employed to render the isosurface in our applications [40]. We will refer to both isolines and isosurfaces as *isomodels* from now on. Under the assumption that the energy of features of interest is the global minimum, the isomodel with the minimum associated energy is chosen as the initialization given a set of predefined isovalues.

A. Initialization

If the model energy of all the possible contours/surfaces defined on the image space could be calculated in a reasonable timeframe, the contour/surface with minimum model energy could be chosen as the solution. Unfortunately, performing an exhaustive search over all the possible models is unrealistic. The new automatic initialization idea introduced in this paper is simple—given a set of candidate models, the desired initialization is the model with the associated minimum model energy within the set. To achieve this goal, (1) computing the model energy for a given model and (2) automatically generating the candidate models are the two key problems. The PIG approach provides a solution to both problems.

First, PIG provides a way to estimate the static external energy from the static external force, which is known. If other energy terms besides the static external energy are quantifiable, the model energy is calculated by adding up all the energy terms. Second, isomodels from the estimated external energy that are close to edges provide excellent candidates for initialization. Since we expect that the final model with correspond in position with image edges, an initial model that is proximal to edges is logical. From an energy point of view, isomodels closer to edges have a lower associated isovalue and, therefore, have a lower associated model external energy. Isomodels can be automatically extracted from the external energy and the model external energy calculation is straightforward, as discussed in the following section.

Given (a) a binary edge map, (b) a static external force, (c) other quantifiable active model energy terms, and (d) candidate models, the PIG automatic initialization method can select the best-choice candidate in terms of minimum model energy as the initialization. Note that the static external force is not necessary edge-based forces, it can be a combination of edge-based forces [19], [32], region-based forces [33], and other forces, as long as they are static forces. The candidate models can be generated automatically by setting isovalues. Other models, such as user defined shapes, can also be included as candidates to integrate priority information.

B. Initialization for Single Active Model

Note that the energy minimization process encourages smaller and larger contours/surfaces for positive value and negative value external energy, respectively. In real applications, the targets of interest are usually of complicated shape with significant boundaries, which suggests using negative value external energy. There may be more than one isomodel that corresponds to a given isovalue. Only the isomodel with the lowest energy is chosen as the optimal initial model. In our implementation, surfaces are represented by triangular meshes,

and contours are represented by connected discrete vertices. Therefore, given the isovalue λ^k , the model energy $\varepsilon^{k,l}$ of the l -th isomodel $\vartheta^{k,l}$ out of all L^k isomodels is calculated by

$$\begin{aligned}\varepsilon^{k,l} &= \int_0^1 \int_0^1 [E_{\text{int}}(\mathbf{v}) + E_{\text{ext}}(\mathbf{v})] d\mathbf{m} d\mathbf{n} \\ &\approx \sum_{i=1}^{n^{k,l}} [E_{\text{int}}(\varphi_i) + E_{\text{ext}}(\varphi_i)] \\ &= \sum_{i=1}^{n^{k,l}} [E_{\text{int}}(\varphi_i) + |\varphi_i|(\lambda^k - E_{\text{max}})] \\ &= \varepsilon_{\text{int}}^{k,l} + (\lambda^k - E_{\text{max}}) \sum_{i=1}^{n^{k,l}} |\varphi_i|\end{aligned}\quad (22)$$

where φ_i denotes the i th face of the triangular mesh, $|\varphi_i|$ denotes the area of φ_i , and $n^{k,l}$ denotes the number of faces of the l th isomodel $\vartheta^{k,l}$. $E_{\text{max}} = \max_{x,y,z} E(x,y,z)$ is the maximum estimated external energy to assure the model external energy is negative.

The model internal energy is defined as

$$\varepsilon_{\text{int}}^{k,l} = \sum_{i=1}^{n^{k,l}} E_{\text{int}}(\varphi_i) \quad (23)$$

the calculation of which is application-dependent and can be found in the Appendix. To measure the internal energy on a discrete triangular mesh for active surfaces is a very complicated and computational expensive process, all the derivations of which can be found in [52] and [53]. For isolines, (22) and (23) also apply, where φ_i denotes the i th edge of the connected contour, $|\varphi_i|$ denotes the length of φ_i , and $n^{k,l}$ denotes the number of edges of the l th isomodel $\vartheta^{k,l}$. The internal energy calculation for active contours is straightforward using a finite difference approximation to estimate the first and second derivatives.

The minimum energy of all L^k isomodels for isovalue λ^k is

$$\varepsilon^k = \min_{1 \leq l \leq L^k} \varepsilon^{k,l}, \quad (24)$$

and the corresponding isomodel is denoted by ϑ^k . Note that a special case occurs when $\alpha = \beta = 0$, i.e., the internal energy can be ignored. Then

$$\begin{aligned}\varepsilon^k &= \min_{1 \leq l \leq L^k} (\lambda^k - E_{\text{max}}) \sum_{i=1}^{n^{k,l}} |\varphi_i| \\ &= (\lambda^k - E_{\text{max}}) \max_{1 \leq l \leq L^k} \sum_{i=1}^{n^{k,l}} |\varphi_i|\end{aligned}\quad (25)$$

which implies that the largest isomodel has the lowest model external energy given isovalue λ^k . Note that $\lambda^k - E_{\text{max}} < 0$ in (25). Given a set of predefined isovalues λ^k , the isomodel with overall minimum model energy is chosen to the initial model. In

2-D, for example an isoline of minimum energy is selected as the initial coarse segmentation. This isoline has two desirable properties that make it an attractive candidate for initialization—(1) low external energy as computed by the PIG method and (2) inherent regularity due to the smoothing of the Poisson equation. Of course, this initialization could be thwarted by intense clutter and problems (gaps) in edge detection.

To summarize, the automatic *single model initialization* procedure is implemented in the following steps.

- i.1. Normalize the force field \mathbf{f} such that the magnitude of all the vectors in the force field is set to 1.
- i.2. Normalize the edge map f to the range $[0, 1]$.
- i.3. Calculate the estimated external energy field E from the external force field \mathbf{f} with Dirichlet boundary conditions computed from edge map f using (19) and (21).
- i.4. Define K isovalues $\{\lambda^k \in [d_0/2, d_1/2], k = 1, 2, \dots, K\}$.
- i.5. For each isovalue λ^k , calculate the minimum model energy ε^k of isomodel ϑ^k using (24).
- i.6. The isomodel ϑ^{k*} of isovalue λ^{k*} yielding the overall minimum model energy is chosen to be the optimal initial model, i.e., $k^* = \arg \min_{1 \leq k \leq K} \varepsilon^k$.

where d_0 denotes the maximum gap between edge fragments, and $d_1 > d_0$ denotes the minimum distance between the edge and noise/clutter. This automatic initialization method can accommodate broken edges, which is exemplified in Fig. 4. The isoline with isovalue d is roughly d pixels away from the edge. Hence, isolines with isovalues less than d_0 are not properly connected, whereas isolines with isovalues larger than d_1 are over-connected. If the selected isovalues λ^k do not belong to $[d_0/2, d_1/2]$, the isolines might pass through the gaps between fragments, or may pass the noise/clutter.

This initialization method incorporates internal energy when selecting isolines in steps i.5 and i.6. Therefore, active models with different internal energy weightings will have different initial models. Additional constraints may be applied to the isomodel selection steps i.5 and i.6 to refine the initialization, such as the selected isomodel must be a closed surface or contour. Different internal energy formulations, such as the energy functional for the shape, size, and position constraints [10], can be employed in (22) to improve the selection of isomodels.

C. Efficient Implementation

The most computationally expensive part of the automatic PIG initialization process is the PIG calculation (step i.3), because (19) involves solving a large linear system. There are many methods to implement the PIG calculation efficiently without sacrificing the quality of the initialized model. The first and most straightforward way is if ω is consisted of several separate regions, each region can be treated as a linear system and calculated separately to reduce the system complexity. For example, it is more efficient to treat the twelve separate regions in Fig. 2(b) as twelve separate linear systems instead of a single large linear system. This method does not modify the estimated external energy field.

Subsampling, the second method, is often necessary (with current PC implementations) in order to calculate the estimated

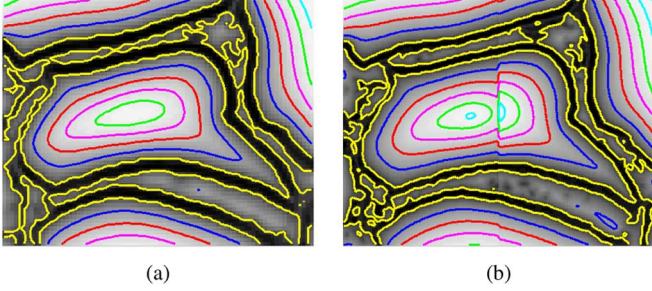


Fig. 3. Estimated external energy field with isolines of the VFC field using (a) the subsampled (by a factor of 2 in each dimension) image, and (b) the left half and right half of Fig. 2(a).

external energy field of 3-D external forces with limited computational resources. The 3-D image, or the volume, can be subsampled to a lower resolution without distorting features of interest, which can considerably reduce the size of the linear system in (19). Although the estimated external energy field after subsampling is not as accurate, the selected initial model should not be significantly affected. If the system is still too large to be computed, the last method available is to divide the volume into several sub-volumes, which are calculated separately. Because of the incompleteness of boundary conditions in each sub-volume, this subdivision method will introduce aliasing between sub-volumes. The two approaches applied to 2-D images are demonstrated in Fig. 3, which shows that subsampling does not significantly alter the initialization, and that image division may cause aliasing between the sub-images, as compared to Fig. 2(f). Although the aliasing effect leads to discontinuity, the isolines close to features of interest still are good approximations and could be used for initialization.

D. Initialization for Multiple Active Models

This automatic initialization process can be easily extended for initializing multiple active models simultaneously. In this section, we proposed two multiple model initialization procedures by modifying steps i.5 and i.6 and incorporating prior information.

The first improved initialization method, termed η -model initialization, is to select η isomodels with lowest model energy for each isovalue, when there are η objects to be segmented in the image. This method is useful in segmenting images with a fixed number of objects, such as medical images where the physical structure is well known. The single model initialization method proposed in Section 6.2.1 can be considered as a special case of η -model initialization with $\eta = 1$, and is termed 1-model initialization. The automatic η -model initialization procedure is implemented in the following steps.

ii.1-4. Same as i.1-4.

ii.5. For each isovalue λ^k , calculate the η -model energy ε^k of the η isomodels with lowest energy $\vartheta^{k,l}, l \in L_\eta^k$

$$\varepsilon^k = \sum_{l \in L_\eta^k} \varepsilon^{k,l} = \sum_{l \in L_\eta^k} \varepsilon_{\text{int}}^{k,l} + (\lambda^k - E_{\text{max}}) \sum_{l \in L_\eta^k} n^{k,l} \quad (26)$$

where L_η^k denotes the indices of the η isomodels with lowest energy for isovalue λ^k . $L_\eta^k = \{1, 2, \dots, L^k\}$ if $L^k < \eta$.

ii.6. The η isomodels $\vartheta^{k*,l}, l \in L_\eta^{k*}$ of the isovalue λ^{k*} yielding the overall minimum η -model energy are selected to initialize η active models such that $k^* = \arg \min_{1 \leq k \leq K} \varepsilon^k$.

Another modified initialization method for multiple models, termed *constrained initialization*, incorporates size and shape constraints in the internal energy and filters the isomodels with the model energy. When prior size and shape information of the objects of interest is available, constrained initialization is similar to η -model initialization except replacing the set of η isomodels with lowest energy L_η^k in step ii.5 and ii.6 by the collection of isomodels with low enough model energy L_c^k .

V. RESULTS AND ANALYSIS

In this section, the proposed PIG initialization method is compared with the center of divergence (CoD) method [23] and the force field segmentation (FFS) method [26]. These two methods represent the competing automatic solutions for active contour initialization in the literature. All methods are implemented in MATLAB 7.0. In each experiment, the active model parameters, including the edge map, the force field, smoothness parameters, and the convergence criteria, are identical for the three methods. Here, *convergence* is defined as the iteration in which the maximum movement across all vertices is less than one half pixel for three consecutive iterations. Further, the term *ground truth* refers to the active model result with high-quality manual initialization. The CoD method needs no extra parameter, and the FFS method requires a threshold to generate binary edge map, which is set equal to τ_f in (21). We apply the Canny edge detector [29] for 2-D examples and the Monga–Deriche edge detector [30] for 3-D examples to obtain edge maps. All experiments employ the VFC field as the external force field due to its superior noise robustness [19], [32], except in Section V.C where GVF [18] is applied.

A. Sensitivity to Broken Edges

We consider a thin 2-D curved region shown in Fig. 4(a) to evaluate the impact of broken edges on the various initialization methods. With this high quality initialization using the PIG single model initialization method, the VFC active contour successfully captures the broken C-shape edges in only 12 iterations, shown in Fig. 4(f). The CoD method initializes 11 active contours, most of which vanish while a single contour captures the inner portion, as shown in Fig. 4(d). The CoD method fails to capture the edges, and requires 70 iterations to converge. The FFS method also fails to initialize active contours correctly in these broken edge examples, since the FFS method treats each connected component in the edge map as a single object and one active contour is formed for each edge fragment. Fig. 4(e)–(f) illustrates that FFS is incapable of accommodating broken edges, whereas the proposed PIG method can handle these scenarios. The first row of Table II summarizes the test results. The PIG method outperforms the other two methods for this example

TABLE II
PERFORMANCE SUMMARY FOR THE CENTER OF DIVERGENCE (CoD) METHOD, THE
FORCE FIELD SEGMENTATION (FFS) METHOD, AND THE PROPOSED PIG METHOD

Example	# of Models Initialized			# of Iterations			Initialization + Deformation = Total CPU Time (sec)			RMSE (pixel)		
	CoD	FFS	PIG	CoD	FFS	PIG	CoD	FFS	PIG	CoD	FFS	PIG
Broken C	11	7	1	70	45	12	0.23+3.13=3.36	0.41+4.02=4.43	1.28+1.82=3.10	3.55	7.36	0.29
Broken Edge Tests (avg. of 11 tests)	1.3	1.8	1.0	113.0	103.0	30.0	0.09+2.99=3.08	0.08+2.86=2.94	0.43+0.83=1.26	1.08	9.62	0.66
Curvature Tests (avg. of 11 tests)	4.2	1.0	1.0	23.5	92.5	12.0	0.03+0.52=0.55	0.11+2.89=3.00	0.20+0.24=0.44	3.04	1.14	0.20
Noise Tests (avg. of 550 tests)	4.8	1.8	1.0	63.5	72.5	33.6	0.04+1.53=1.57	0.11+3.14=3.25	0.04+0.88=0.92	2.89	2.40	1.52
2D Prostate Ultrasound	148	2	1	1125	425	205	0.92+160=161	6.93+61.9=68.8	5.26+24.7=29.9	1.76	61.1	0.55
2D Lungs MRI	130	48	2	345	375	48	1.05+132=133	9.25+133=142	7.77+14.9=22.7	0.29	18.1	0.39
2D Cells	89	20	6	246	171	18	0.48+49.0=49.5	2.20+36.7=38.9	2.49+3.38=5.87	0.40	1.08	0.26
3D Prostate Ultrasound	3	1	1	105	45	20	0.31+426=426	21.4+319=340	31.2+71.1=102	2.03	0.50	0.45
3D Bone MRI	356	1	1	132	160	82	5.13+611=616	107+3021=3128	78.4+373=451	1.41	3.61	0.61
3D Heart MRI	545	1	3	104	128	16	9.47+232=241	208+437=645	274+236=510	68.2	35.8	1.16

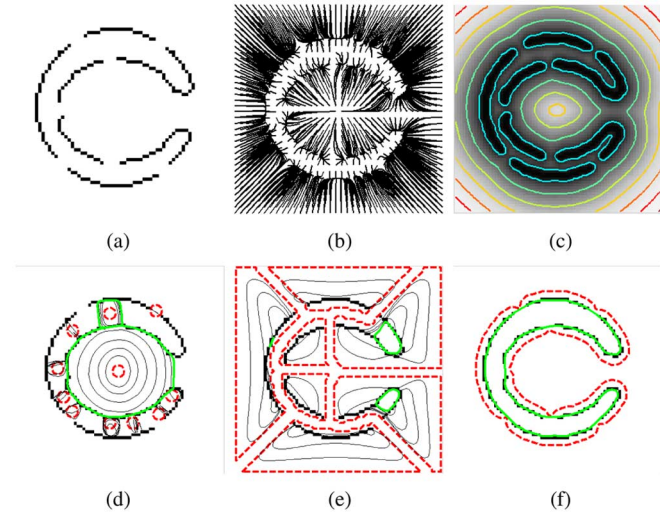


Fig. 4. (a) Broken edges for a thin, curved region. (b) The VFC force field and (c) corresponding estimated external energy field overlapped with isolines. The initial (red dashed lines) and final (green solid lines) active contours using (d) the CoD method, (e) the FFS method, and (f) the PIG single model initialization method.

in terms of correct number of models initialized, iterations needed for convergence, computing time, and segmentation accuracy.

Additionally, we generate numerous geometric shapes of increasing gap width between edge fragments shown in Fig. 5 to evaluate the impact of broken edges on the various initialization methods. The segmentation accuracy is measured by the root mean squared error (RMSE) between the active contour result and the ground truth. The results using the CoD method are calculated after region merging.

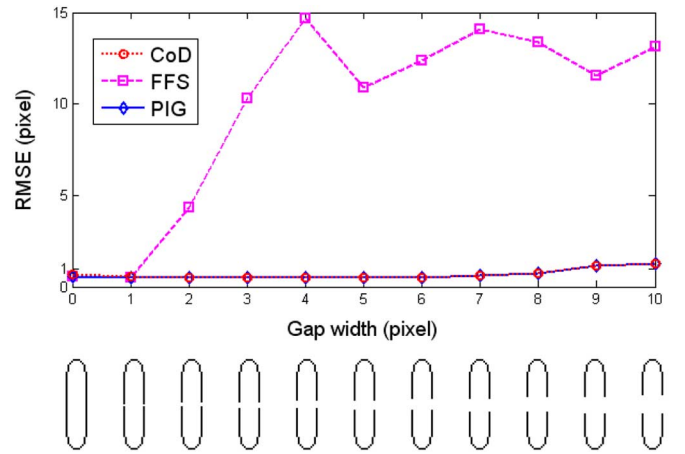


Fig. 5. RMSE of active contours using the CoD method, the FFS method and the PIG method for shapes with increasing gap width between edge fragments as shown below the plot.

In these synthetic tests, the CoD and PIG methods both successfully capture the objects with broken edges, whereas the FFS method fails when the gap width is larger than 2 pixels. Because the FFS method always initializes one model for each connected component in the edge map, two models initialized by the FFS method collapse to the edge fragments in a few iterations. As may be observed in Table II, the PIG method requires only 30 iterations on average to converge, which is much less than the 100+ iterations required by the other two methods. Note that each iteration has exactly the same settings and associated expense for all three methods.

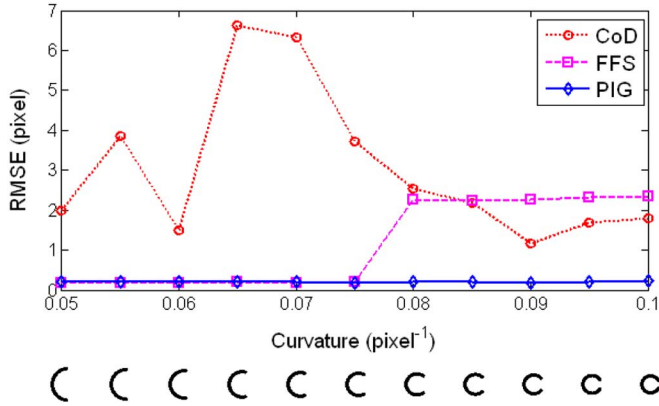


Fig. 6. RMSE of active contours using the CoD method, the FFS method and the PIG method for shapes with increasing curvature as shown below the plot.

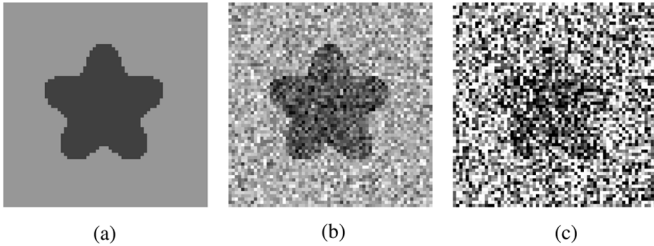


Fig. 7. (a) Noise-free image. Example noise corrupted images with (b) 5 dB SNR and (c) -5 dB SNR. (a) SNR = ∞ dB, (b) SNR = 5 dB, and (c) SNR = -5 dB.

B. Sensitivity to Curvature

We generate numerous geometric shapes of increasing curvature shown in Fig. 6 to evaluate the impact of curvature on the various initialization methods. The CoD method initializes several models inside the shape and fails to segment the entire shape correctly. The active contours using the FFS method are successful for the low curvature shapes, but fail to capture the high curvature shapes and are stuck at the local minima. Because the FFS method always initializes the model outside the object, the small gap between the two ends of the high curvature shapes prevents the active contour from moving into the deep concavity. Only the PIG method exhibits consistent performance for shapes with varying curvature, as shown in Fig. 6. The contrast is also dramatic in computational cost—the average number of iterations required for convergence is 12.0 for the PIG method, as compared to 92.5 for the FFS method.

C. Sensitivity to Noise

To evaluate the impact of noise on the various initialization methods, we generate 50 images with the same SNR for 11 different SNR levels (550 images in total) by randomly adding zero mean Gaussian noise to a star-shaped grayscale image as shown in Fig. 7(a). Two examples with 5 dB SNR and -5 dB SNR are shown in Fig. 7(b) and (c). We use the GVF field in this experiment to accentuate the effect of noise on the segmentation process. The active contour result obtained from the noise-free image is taken as the ground truth. By examining Fig. 8, we can see that the CoD method and the FFS method tend to initialize

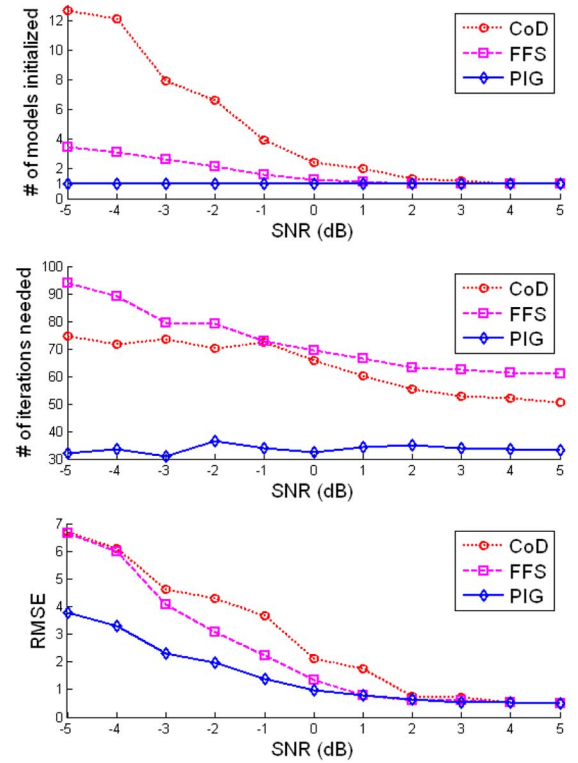


Fig. 8. (Top) Average number of models initialized, (middle) the average number of iterations needed, and (bottom) the average RMSE of three initialization methods at different SNR levels. All values at each level are averaged over 50 synthetic images generated by randomly adding Gaussian noise to the noise-free image. The parameters of active models are identical for all three methods.

more models as the SNR decreases, because there are more centers of divergence and edge fragments with lower SNR. The PIG single model initialization method, however, only selects a single optimal isomodel as the initial model. The active contours using the PIG method need smaller number of iterations to converge because the initial model is closer to features of interest. The PIG method also outperforms the other two methods in segmentation accuracy as measured by RMSE, as shown in Fig. 8. The difference in performance is explained by the fact that the CoD method and the FFS method initialize the models far away from features of interest where the active model may be easily distracted by the noise.

D. Active Contours for 2-D Real Images

To demonstrate the effectiveness of the proposed PIG initialization method on real datasets, we compare the performance of three initialization methods on 2-D biomedical images. Fig. 9(a) demonstrates a typical ultrasound image of a human prostate. Speckle reducing anisotropic diffusion (SRAD) is employed to smooth the ultrasound images prior to segmentation [54]. The edge map and the VFC external force are calculated from the processed image. After thresholding the edge map using (21) and applying an area close morphological filter to eliminate small features, the region Ω is obtained. The estimated external energy field overlapped with the isolines is demonstrated in Fig. 9(f). Fig. 9(c)–(e) shows that an active contour is initialized by

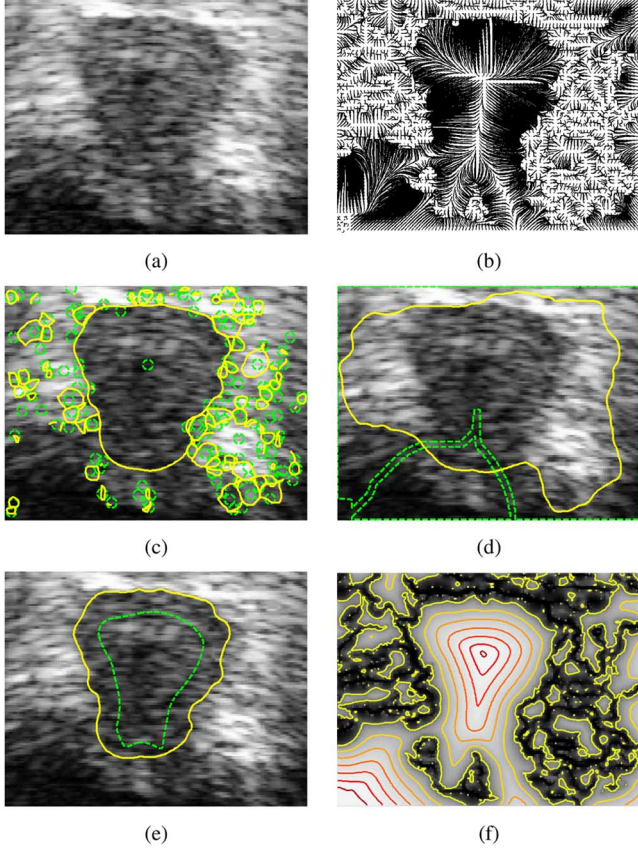


Fig. 9. (a) Ultrasound image of a human prostate. (b) Streamlines generated from the VFC external force field. The initial (green dashed line) and final (yellow solid line) active contours using (c) the CoD method, (d) the FFS method, and (e) the PIG single model initialization method. (f) The estimated external energy field of the VFC field overlapped with isolines.

the optimal closed isoline using the 1-model initialization method and accurately captures the prostate boundary in 205 iterations, whereas the CoD method needs 1125 iterations to achieve a similar result with 148 models initialized, and the FFS method fails to segment the correct boundary. Because there are a large number of edges surrounding features of interest, the CoD method initializes redundant models, and the active contours initialized outside the object using the FFS method are blocked by those edges. Fig. 9 is another example to show that the proposed method accommodates broken edges.

A lung MR image [55] is chosen to exemplify the effectiveness of η -model initialization shown in Fig. 10. After calculation of the estimated external energy field from the VFC field, two active contours are initialized by the 2-model initialization method, as shown in Fig. 10(b), (e), and (f). The active contours segment both the left lung and the right lung precisely in merely 48 iterations, compared to the over 300 iterations required for the other two methods. As with the previous example, the CoD method reaches a similar result with the cost of additional models (130 versus 2 for PIG) initialized and larger number of iterations needed. The FFS method fails again due to the broken edges caused by noise. This is the only example where the PIG method does not yield the lowest RMSE.

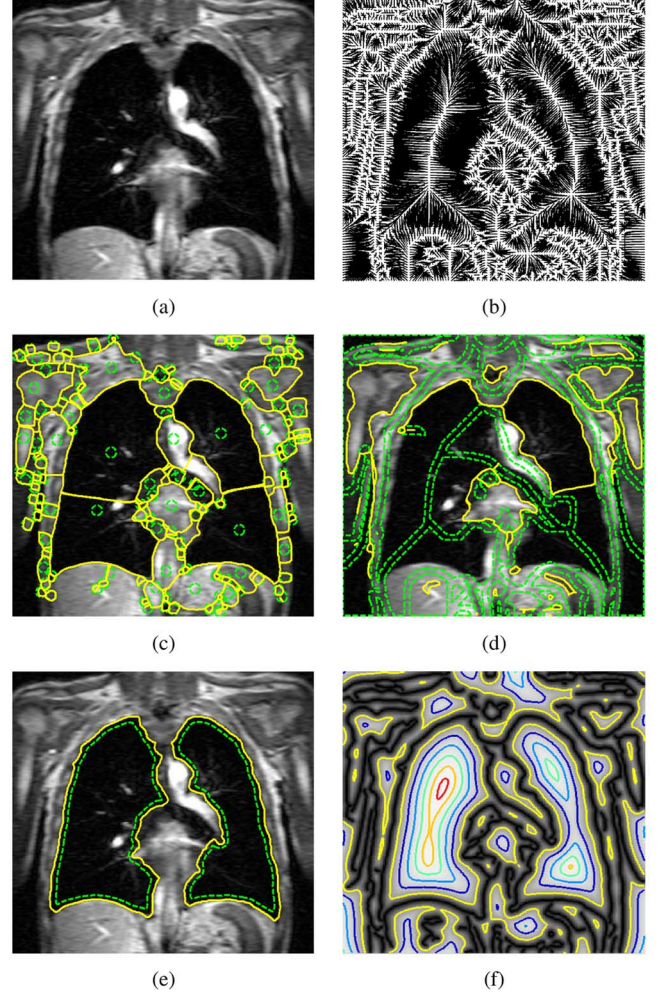


Fig. 10. (a) MR image slice of a human lung. (b) Streamlines generated from the VFC external force field. The initial (green dashed lines) and final (yellow solid lines) active contours using (c) the CoD method, (d) the FFS method, and (e) the PIG 2-model initialization method. (f) The estimated external energy field of the VFC field superposed with isolines.

As shown in Table II, the CoD method yields a slightly lower RMSE (0.29 pixels) than the PIG method (0.39 pixels).

A microscopic image of leukocytes *in vivo* shown in Fig. 11 is used to evaluate the constrained initialization method. Since the leukocytes are circular in shape, and the leukocyte radii are known for a given resolution, we employ energy terms for circular shape and size constraints in this example [10]. The model energy $\varepsilon^{k,l}$ is calculated by

$$\varepsilon^{k,l} = \varepsilon_{\text{int}}^{k,l} + (\lambda^k - E_{\text{max}}) \sum_{i=1}^{n^{k,l}} |\varphi_i| + w_{\text{shape}} \varepsilon_{\text{shape}}^{k,l} + w_{\text{size}} \varepsilon_{\text{size}}^{k,l} \quad (27)$$

where $\varepsilon_{\text{shape}}^{k,l}$ and $\varepsilon_{\text{size}}^{k,l}$ are energy terms for shape and size constraints, respectively, and w_{shape} and w_{size} are corresponding weighting parameters. The calculation of these energy terms is discussed in the Appendix. As demonstrated in Fig. 11(e), all six bright leukocytes are accurately initialized and segmented by the VFC active contours in only 18 iterations using the constrained initialization method. Both the CoD method and the

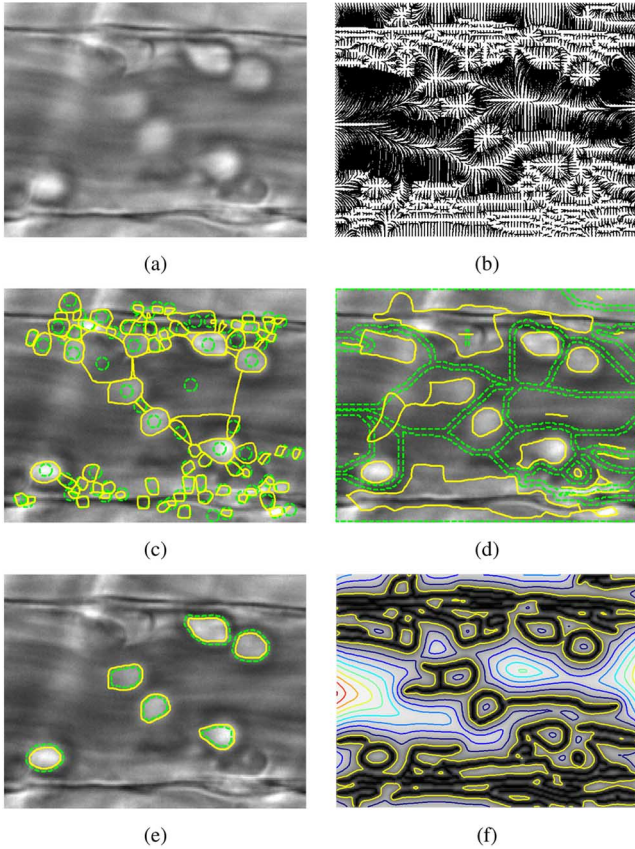


Fig. 11. (a) Microscopic image of leukocytes in a blood venule. (b) Streamlines generated from the VFC external force field. The initial (green dashed lines) and final (yellow solid lines) active contours using (c) the CoD method, (d) the FFS method, and (e) the PIG constrained initialization method. (f) The estimated external energy field of the VFC field superposed with isolines.

FFS method initialize more models than desired and require more than 170 iterations to converge. In addition, the active contours initialized by FFS fail to capture the top-left and bottom-right leukocytes correctly. The PIG method yields the most accurate segmentation result in terms of lowest RMSE, as shown in Table II.

E. Active Surfaces for 3-D Real Images

We now demonstrate examples employing VFC active surfaces with the proposed automatic PIG initialization method in 3-D. We also extend the CoD method and the FFS method to 3-D images, in order to compare them with the PIG method.

The VFC active surface with single model initialization is applied to a 3-D elastography ultrasound image of prostate lesion [56]. As shown in Fig. 12(c), since the selected iso-surface is close to features of interest, the VFC active surface converges in only 20 iterations. In contrast, the active surface requires 105 and 45 iterations to converge if initialized using the CoD method and the FFS method, respectively. Note that these surface updates also necessitate complicated surface remeshing [27], which explains why the computation time is 4 times longer even though the number of iterations only doubles for the FFS method. Two of the three VFC active surfaces initialized by the CoD method vanish after several

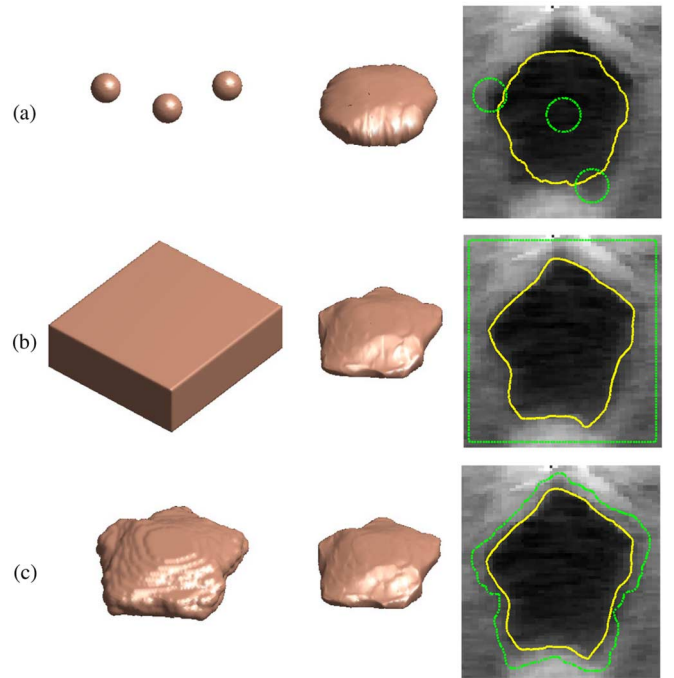


Fig. 12. (Right column) Intersection of the middle image slice of a 3-D ultrasound image of the prostate with (left column) the initial and (middle column) the final VFC active surfaces in green dashed lines and yellow solid lines, respectively, using (a) the CoD method, (b) the FFS method, and (c) the PIG single model initialization method.

iterations, and the remaining surface fails to capture features of interest accurately. The center slice of the original 3-D image overlapped with the intersection of the initial and final active surfaces are also demonstrated in Fig. 12. The PIG method provides the lowest RMSE (0.45 pixels) across three methods shown in Table II.

The single model initialization method is also applied to the 3-D MR image of a cadaver human ankle [57], as shown in Fig. 13(c). The VFC active surface converges to the talus bone boundary accurately in 82 iterations using the PIG initialization method, whereas over 130 deformations and surface remeshing are required using the other two methods. As shown in Fig. 13(a), the CoD method initializes 356 models, only one of which does not collapse and coarsely captures features of interest. Similar to the 2-D prostate example shown in Fig. 9, the FFS method initializes a cube-like active surface outside the object, which is distracted by the edges surrounding the object. Two slices of the original 3-D MR image overlapped with the intersection of the initial and final VFC active surfaces are also demonstrated in Fig. 13.

To segment cardiac borders from a 3-D MR image of an *ex vivo* canine heart, we employ the 3-model initialization method for VFC active surfaces. The VFC active surfaces converge to the endocardial and epicardial borders accurately in only 16 iterations, as shown in Fig. 14. The CoD method initializes 545 models, all of which vanish after 104 iterations. The FFS method forms only one active surface outside the heart, and captures only part of the epicardial border after 128 surface deformations and remeshing. The short axis and long axis slices overlapped with the segmentation results are demonstrated in Fig. 14(c)–(f).

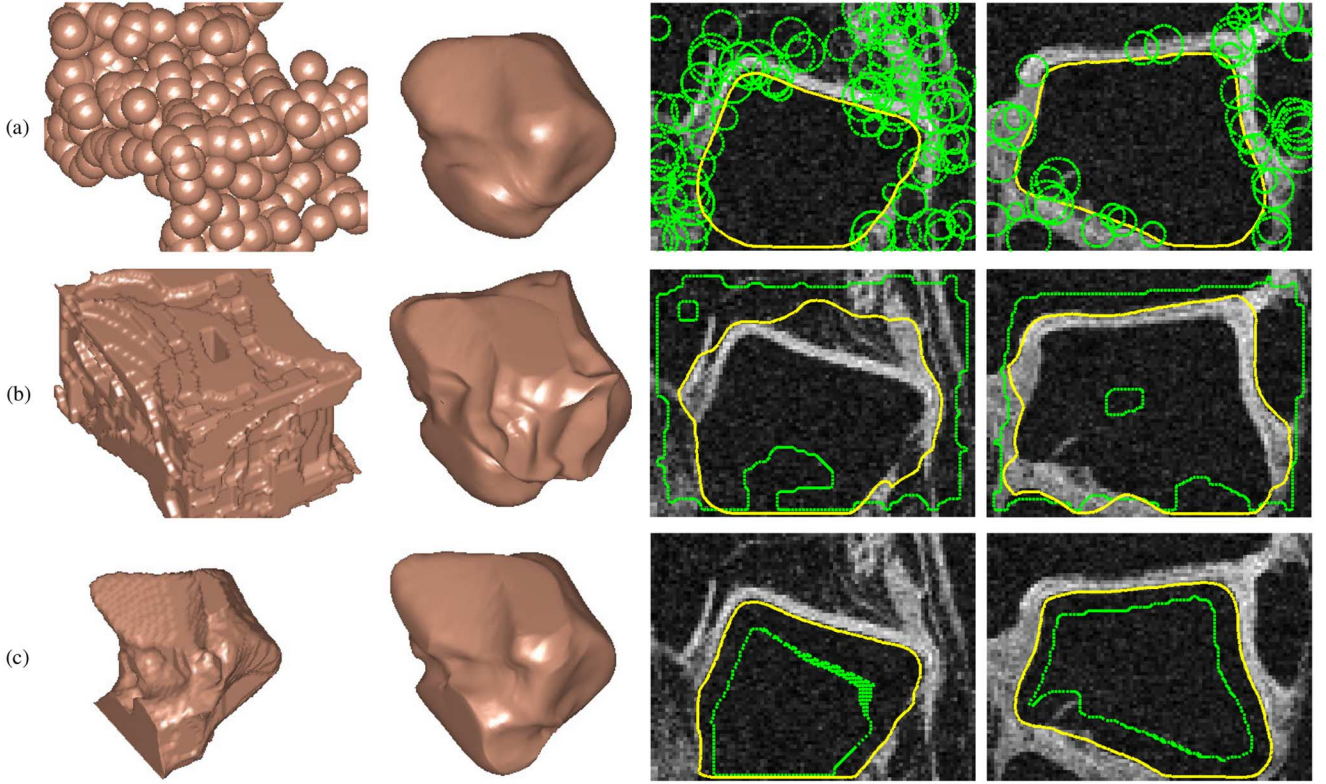


Fig. 13. Intersection of (left column) the initial and (second left column) the final VFC active surfaces with (right two columns) two selected image slices in green dashed lines and yellow solid lines, respectively, using (a) the CoD method, (b) the FFS method, and (c) the PIG single model initialization method.

As shown in Table II, the PIG method yields a significantly smaller RMSE than the CoD and FFS methods.

F. Summary

We summarize all ten examples in Table II. The results for the broken edge and curvature examples are averaged over all 11 images, and the results for the noise example are averaged over 550 images.

The PIG method initializes a predefined number of models, whereas the CoD method tends to initialize more than desired number of models. The FFS method initializes one model for each connected component in the binary edge map, which leads to over-initialization of active models for objects with broken edges, and under-initialization for multiple objects in which the edges are connected. Because the initial models using the PIG method are closer to features of interest, the PIG method requires a significantly smaller number of iterations for the active models to converge compared to the CoD method and the FFS method. As a result, although the initialization time of the PIG method is the highest, this is offset by a lower number of required iterations. Thus, the total computing time of the PIG method is the lowest of the three candidates. Additionally, the PIG method provides superior segmentation accuracy over the other two methods.

VI. CONCLUSION

In this paper, a novel automatic initialization approach for parametric active models, termed the Poisson inverse gradient

(PIG) initialization method, has been introduced. The PIG technique estimates the underlying external energy field from the external force field via solving Poisson's equation, which can also be used for vector field visualization. From the estimated external energy field, isomodels are extracted, and the isomodel with the lowest energy is selected as the initial model. To obtain a high quality initialization, both an advanced edge detector and a noise robust external force field are necessary.

This novel method can initialize one or more active models automatically in both 2-D and 3-D. Efficient implementation schemes are proposed to reduce the computational cost. We also provided guidelines for selecting isovalues. Several beneficial properties of the PIG method were demonstrated by a set of examples and comparisons with the CoD and FFS initialization methods. We have shown that the PIG method excels in terms of robustness to noise, accommodation of broken edges and multiple objects, choice of number of models deployed, accurate segmentation, and rapid convergence to features of interest.

The PIG initialization method is most suitable for active models that are dominated by a static external force, from which the external energy can be estimated. The shortcoming of the method is that the PIG technique may fail when the maximum distance between edge fragments is larger than the minimum distance between the edge and noise/clutter. The design of an optimally efficient implementation of PIG initialization is an open research problem. Although this method is currently

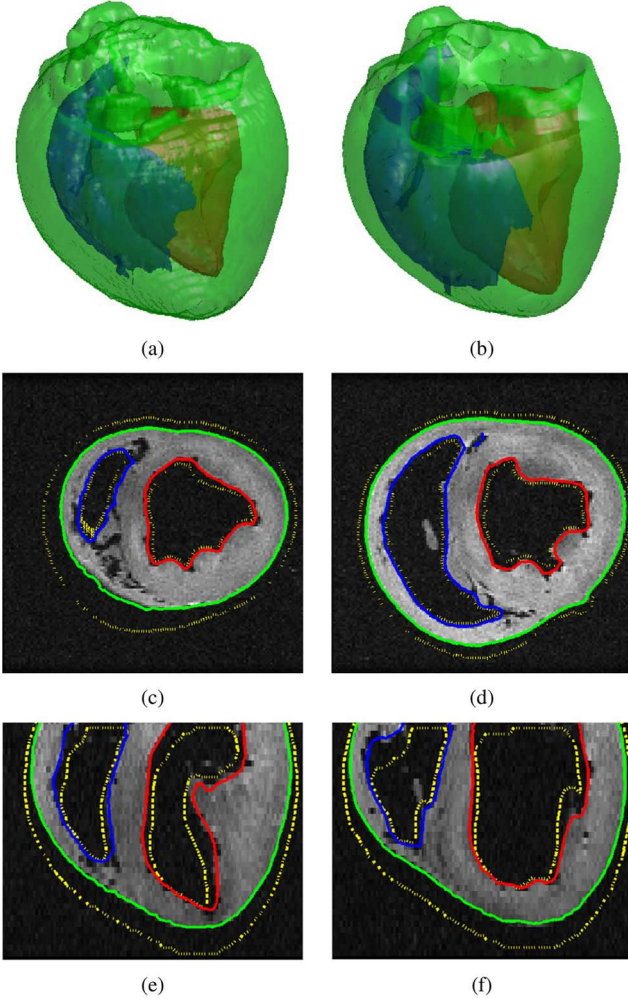


Fig. 14. (a) Three selected isosurfaces of the estimated external energy field from the VFC field of a 3-D canine heart MR image. (b) The VFC active surfaces deformed from the isosurfaces after 12 iterations to segment the left ventricle (red), right ventricle (blue) and epicardial (green) borders. The intersection of (c), (d) two selected short axis slices and (e), (f) two selected long axis slices with the selected isosurfaces (yellow dashed lines) and the VFC active surfaces (green, red and blue solid lines).

limited to parametric active models, we are investigating the extension of this method to geometric active models.

APPENDIX

A. Active Contour Internal Energy Calculation

A typical internal energy of active contour $\mathbf{v}(s) = [x(s), y(s)]^T$, $s \in [0, 1]$ is given as

$$E_{\text{int}}(\mathbf{v}) = \frac{1}{2}(\alpha|\mathbf{v}'(s)|^2 + \beta|\mathbf{v}''(s)|^2) \quad (28)$$

where $\mathbf{v}'(s)$ and $\mathbf{v}''(s)$ are the first and second derivatives of $\mathbf{v}(s)$ with respect to s . After the continuous contour $\mathbf{v}(s)$ is uniformly sampled and represented by a set of M_{ac} discrete vertices $\mathbf{v}_i, i = 0, 1, \dots, M_{\text{ac}} - 1$ and M_{ac} edges φ_i with length $|\varphi_i|$ that connect \mathbf{v}_i and \mathbf{v}_{i+1} . Assuming the second derivatives are constant, which implies the first derivatives are linear, on each

edge, the model internal energy can be calculated using finite difference approximation

$$\begin{aligned} \varepsilon_{\text{int}} &= \sum_{i=0}^{M_{\text{ac}}-1} E_{\text{int}}(\varphi_i) \\ &= \frac{1}{2} \sum_{i=0}^{M_{\text{ac}}-1} |\varphi_i| \left(\alpha \left| \frac{\mathbf{v}'_{i+1} + \mathbf{v}'_i}{2} \right|^2 + \beta \left| \frac{\mathbf{v}'_{i+1} - \mathbf{v}'_i}{|\varphi_i|/\Phi} \right|^2 \right) \\ &= \frac{\alpha}{8} \sum_{i=0}^{M_{\text{ac}}-1} |\varphi_i| |\mathbf{v}'_{i+1} + \mathbf{v}'_i|^2 \\ &\quad + \frac{\beta\Phi^2}{2} \sum_{i=0}^{M_{\text{ac}}-1} \frac{1}{|\varphi_i|} |\mathbf{v}'_{i+1} - \mathbf{v}'_i|^2 \end{aligned} \quad (29)$$

where “+” and “−” in the subscripts denote modulo M_{ac} addition and subtraction to accommodate the periodic boundary condition of a closed contour, and

$$\Phi = \sum_{i=0}^{M_{\text{ac}}-1} |\varphi_i| \quad (30)$$

denotes the overall length of the contour. Note that

$$|\mathbf{v}'_{i+1} \pm \mathbf{v}'_i|^2 = |\mathbf{v}'_{i+1}|^2 + |\mathbf{v}'_i|^2 \pm 2\mathbf{v}'_{i+1} \cdot \mathbf{v}'_i \quad (31)$$

where \cdot denotes the dot product, and the contour is uniformly sampled, i.e., $|\varphi_i| = |\varphi_0|$ and $\Phi = M_{\text{ac}}|\varphi_0|$, (29) can be simplified using the periodic boundary condition

$$\begin{aligned} \varepsilon_{\text{int}} &= \frac{\alpha}{8} |\varphi_0| \sum_{i=0}^{M_{\text{ac}}-1} |\mathbf{v}'_{i+1} + \mathbf{v}'_i|^2 \\ &\quad + \frac{\beta}{2} M_{\text{ac}}^2 |\varphi_0| \sum_{i=0}^{M_{\text{ac}}-1} |\mathbf{v}'_{i+1} - \mathbf{v}'_i|^2 \\ &= \frac{|\varphi_0|}{4} \sum_{i=0}^{M_{\text{ac}}-1} [\alpha \mathbf{v}'_i \cdot (\mathbf{v}'_i + \mathbf{v}'_{i+1}) \\ &\quad + 4\beta M_{\text{ac}}^2 \mathbf{v}'_i \cdot (\mathbf{v}'_i - \mathbf{v}'_{i+1})] \end{aligned} \quad (32)$$

where \mathbf{v}'_i can be approximated by finite difference

$$\mathbf{v}'_i = \frac{\mathbf{v}_{i+1} - \mathbf{v}_{i-1}}{(|\varphi_i| + |\varphi_{i-1}|)/\Phi} = \frac{M_{\text{ac}}}{2} (\mathbf{v}_{i+1} - \mathbf{v}_{i-1}). \quad (33)$$

Finally, (32) can be written as

$$\begin{aligned} \varepsilon_{\text{int}} &= \alpha M_{\text{ac}}^2 \frac{|\varphi_0|}{16} \sum_{i=0}^{M_{\text{ac}}-1} (\mathbf{v}_{i+1} - \mathbf{v}_{i-1}) \\ &\quad \cdot (\mathbf{v}_{i+1} - \mathbf{v}_{i-1} + \mathbf{v}_{i+2} - \mathbf{v}_i) \\ &\quad + \beta M_{\text{ac}}^4 \frac{|\varphi_0|}{4} \sum_{i=0}^{M_{\text{ac}}-1} (\mathbf{v}_{i+1} - \mathbf{v}_{i-1}) \\ &\quad \cdot (\mathbf{v}_{i+1} - \mathbf{v}_{i-1} - \mathbf{v}_{i+2} + \mathbf{v}_i) \\ &= \alpha M_{\text{ac}}^2 \frac{|\varphi_0|}{16} \sum_{i=0}^{M_{\text{ac}}-1} \mathbf{v}_i \\ &\quad \cdot (2\mathbf{v}_i + \mathbf{v}_{i+1} - 2\mathbf{v}_{i+2} - \mathbf{v}_{i+3}) \\ &\quad + \beta M_{\text{ac}}^4 \frac{|\varphi_0|}{4} \sum_{i=0}^{M_{\text{ac}}-1} \mathbf{v}_i \\ &\quad \cdot (2\mathbf{v}_i - \mathbf{v}_{i+1} - 2\mathbf{v}_{i+2} + \mathbf{v}_{i+3}). \end{aligned} \quad (34)$$

B. Shape and Size Constraints Energy Calculation

The energy for circular shape constraint is given as [10]

$$E_{\text{shape}}(\mathbf{v}) = \frac{1}{2} |\mathbf{v}(s) - \bar{\mathbf{v}} - \bar{R}\mathbf{e}(s)|^2 \quad (35)$$

where

$$\bar{\mathbf{v}} = \int_0^1 \mathbf{v}(s) ds \quad (36)$$

is the active contour center

$$\bar{R} = \int_0^1 |\mathbf{v}(s) - \bar{\mathbf{v}}| ds \quad (37)$$

is the mean radius, and $\mathbf{e}(s) = [\cos(2\pi s), \sin(2\pi s)]^T$. After uniformly sampling, assuming the shape energy is linear on each edge, the model shape energy can be calculated using finite difference approximation

$$\begin{aligned} \varepsilon_{\text{shape}} &= \sum_{i=0}^{M_{\text{ac}}-1} E_{\text{shape}}(\varphi_i) \\ &= \sum_{i=0}^{M_{\text{ac}}-1} \frac{|\varphi_i|}{2} [E_{\text{shape}}(\mathbf{v}_i) + E_{\text{shape}}(\mathbf{v}_{i+1})] \\ &= |\varphi_0| \sum_{i=0}^{M_{\text{ac}}-1} E_{\text{shape}}(\mathbf{v}_i) \\ &= \frac{|\varphi_0|}{2} \sum_{i=0}^{M_{\text{ac}}-1} |\mathbf{v}_i - \bar{\mathbf{v}} - \bar{R}\mathbf{e}_i|^2 \end{aligned} \quad (38)$$

where

$$\begin{aligned} \bar{\mathbf{v}} &= \frac{1}{M_{\text{ac}}} \sum_{i=0}^{M_{\text{ac}}-1} \mathbf{v}_i, \\ \bar{R} &= \frac{1}{M_{\text{ac}}} \sum_{i=0}^{M_{\text{ac}}-1} |\mathbf{v}_i - \bar{\mathbf{v}}|, \\ \mathbf{e}_i &= [\cos(2\pi i/M_{\text{ac}}), \sin(2\pi i/M_{\text{ac}})]^T. \end{aligned} \quad (39)$$

Then the calculation of the model size energy is straightforward [10]

$$\varepsilon_{\text{size}} = \frac{1}{2} (\bar{R} - K)^2 \quad (40)$$

where K is the expected radius defined by the user.

C. Active Surface Internal Energy Calculation

A typical internal energy of active surfaces $\mathbf{v}(m, n) = [x(m, n), y(m, n), z(m, n)]^T$, $(m, n) \in [0, 1]^2$ is given as

$$E_{\text{int}}(\mathbf{v}) = \frac{1}{2} \left(\alpha \sum_a \left| \frac{\partial \mathbf{v}}{\partial a} \right|^2 + \beta \sum_{a,b} \left| \frac{\partial^2 \mathbf{v}}{\partial a \partial b} \right|^2 \right) \quad (41)$$

where the first term is referred as *thin membrane energy* and the second term is referred as *thin plate energy*. To measure the internal energy on a discrete triangular mesh is a complicated and computational expensive process. The major challenge is to find an appropriate parameterization for the triangular mesh to approximate the first and second partial derivatives closely. All the derivations and equations can be found in [52] and [53]. The internal energy calculation by way of a different definition, such as an energy including curvature terms, could be achieved by computing geometric characteristics [58].

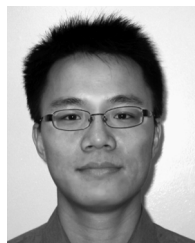
ACKNOWLEDGMENT

The authors would like to thank Dr. P. A. Helm, Dr. R. L. Winslow, and Dr. E. McVeigh for the 3-D canine heart MR data, Dr. J. Hossack for the ultrasound data, and Dr. C. Li for valuable conversations.

REFERENCES

- [1] M. Kass, A. Witkin, and D. Terzopoulos, "Snakes—Active contour models," *Int. J. Comput. Vis.*, vol. 1, pp. 321–331, 1987.
- [2] D. Terzopoulos, A. Witkin, and M. Kass, "Constraints on deformable models—Recovering 3D shape and nonrigid motion," *Artif. Intell.*, vol. 36, pp. 91–123, 1988.
- [3] M. Gastaud, M. Barlaud, and G. Aubert, "Combining shape prior and statistical features for active contour segmentation," *IEEE Trans. Circuits Syst. Video Technol.*, vol. 14, no. 5, pp. 726–734, May 2004.
- [4] J.-O. Lachaud and A. Montanvert, "Deformable meshes with automated topology changes for coarse-to-fine three-dimensional surface extraction," *Med. Image Anal.*, vol. 3, pp. 187–207, 1999.
- [5] T. McInerney and D. Terzopoulos, "Topology adaptive deformable surfaces for medical image volume segmentation," *IEEE Trans. Med. Process.*, vol. 18, no. 10, pp. 840–850, Oct. 1999.
- [6] T. McInerney and D. Terzopoulos, "A dynamic finite element surface model for segmentation and tracking in multidimensional medical images with application to cardiac 4D image analysis," *Comput. Med. Imag. Graph.*, vol. 19, pp. 69–83, 1995.
- [7] J. Cheng and S. W. Foo, "Dynamic directional gradient vector flow for snakes," *IEEE Trans. Image Process.*, vol. 15, no. 6, pp. 1563–1571, Jun. 2006.
- [8] J. Bredno, T. M. Lehmann, and K. Spitzer, "A general discrete contour model in two, three, and four dimensions for topology-adaptive multichannel segmentation," *IEEE Trans. Pattern Anal. Mach. Intell.*, vol. 25, no. 5, pp. 550–563, May 2003.
- [9] N. Ray and S. T. Acton, "Motion gradient vector flow: An external force for tracking rolling leukocytes with shape and size constrained active contours," *IEEE Trans. Med. Imag.*, vol. 23, no. 12, pp. 1466–1478, Dec. 2004.
- [10] N. Ray, S. T. Acton, and K. Ley, "Tracking leukocytes in vivo with shape and size constrained active contours," *IEEE Trans. Med. Imag.*, vol. 21, no. 10, pp. 1222–1235, Oct. 2002.
- [11] N. Paragios and R. Deriche, "Geodesic active contours and level sets for the detection and tracking of moving objects," *IEEE Trans. Pattern Anal. Mach. Intell.*, vol. 22, no. 3, pp. 266–280, Mar. 2000.
- [12] S. T. Acton and N. Ray, *Biomedical Image Analysis: Tracking*, A. C. Bovik, Ed. San Rafael, CA: Morgan and Claypool, 2006.
- [13] A. R. Mansouri, D. P. Mukherjee, and S. T. Acton, "Constraining active contour evolution via lie groups of transformation," *IEEE Trans. Image Process.*, vol. 13, no. 6, pp. 853–863, Jun. 2004.
- [14] T. F. Cootes, G. J. Edwards, and C. J. Taylor, "Active appearance models," *IEEE Trans. Pattern Anal. Mach. Intell.*, vol. 23, no. 6, pp. 681–685, Jun. 2001.
- [15] J. A. Sethian, *Level Set Methods and Fast Marching Methods: Evolving Interfaces in Computational Geometry, Fluid Mechanics, Computer Vision, and Materials Science*. Cambridge, U.K.: Cambridge Univ. Press, 1999.
- [16] D. Terzopoulos and T. McInerney, "Deformable models in medical image analysis: A survey," *Med. Image Anal.*, vol. 1, pp. 91–108, 1996.
- [17] T. F. Chan and L. A. Vese, "Active contours without edges," *IEEE Trans. Image Process.*, vol. 10, no. 2, pp. 266–277, Feb. 2001.
- [18] C. Xu and J. L. Prince, "Snakes, shapes, and gradient vector flow," *IEEE Trans. Image Process.*, vol. 7, no. 3, pp. 359–369, Mar. 1998.

- [19] B. Li and S. T. Acton, "Active contour external force using vector field convolution for image segmentation," *IEEE Trans. Image Process.*, to be published.
- [20] W. Neuenschwander, P. Fua, G. Szekely, and O. Kubler, "Initializing snakes," presented at the IEEE Conf. Computer Vision and Pattern Recognition, Seattle, WA, 1994, unpublished.
- [21] L. D. Cohen and R. Kimmel, "Global Minimum for Active Contour Models: A Minimal Path Approach," *Int. J. Comput. Vis.*, vol. 24, pp. 57–78, 1997.
- [22] R. Ardon and L. D. Cohen, "Fast Constrained Surface Extraction by Minimal Paths," *Int. J. Comput. Vis.*, vol. 69, pp. 127–136, 2006.
- [23] X. Ge and J. Tian, "An automatic active contour model for multiple objects," presented at the Int. Conf. Pattern Recognition, 2002, unpublished.
- [24] Y. He, Y. Luo, and D. Hu, "Semi-automatic initialization of gradient vector flow snakes," *J. Electron. Imag.*, vol. 15, p. 043006, 2006.
- [25] C. Tauber, H. Batatia, and A. Ayache, "A general quasi-automatic initialization for snakes: Application to ultrasound images," presented at the IEEE Int. Conf. Image Processing, 2005, unpublished.
- [26] C. Li, J. Liu, and M. D. Fox, "Segmentation of external force field for automatic initialization and splitting of snakes," *Pattern Recognit.*, vol. 38, pp. 1947–1960, 2005.
- [27] J.-Y. Park, T. McInerney, D. Terzopoulos, and M.-H. Kim, "A non-self-intersecting adaptive deformable surface for complex boundary extraction from volumetric images," *Comput. Graph.*, vol. 25, pp. 421–440, 2001.
- [28] L. D. Cohen and I. Cohen, "Finite-element methods for active contour models and balloons for 2-D and 3-D images," *IEEE Trans. Pattern Anal. Mach. Intell.*, vol. 15, no. 11, pp. 1131–1147, Nov. 1993.
- [29] J. Canny, "A computational approach to edge detection," *IEEE Trans. Pattern Anal. Mach. Intell.*, vol. PAMI-8, no. 6, pp. 679–714, Nov. 1986.
- [30] O. Monga, R. Deriche, G. Malandain, and J. P. Cocquerez, "Recursive filtering and edge tracking: Two primary tools for 3D edge detection," *Image Vis. Comput.*, vol. 9, pp. 203–214, 1991.
- [31] C. Xu, D. L. Pham, M. E. Rettmann, D. N. Yu, and J. L. Prince, "Reconstruction of the human cerebral cortex from magnetic resonance images," *IEEE Trans. Med. Process.*, vol. 18, no. 6, pp. 467–480, Jun. 1999.
- [32] B. Li and S. T. Acton, "Vector field convolution for image segmentation using snakes," presented at the IEEE Int. Conf. Image Processing, Atlanta, GA, 2006, unpublished.
- [33] X. Xie and M. Mirmehdi, "RAGS: region-aided geometric snake," *IEEE Trans. Image Process.*, vol. 13, no. 5, pp. 640–652, Jun. 2004.
- [34] T. McInerney and D. Terzopoulos, "T-Snakes: Topology adaptive snakes," *Med. Image Anal.*, vol. 4, pp. 73–91, 2000.
- [35] W. Neuenschwander, P. Fua, G. Szekely, and O. Kubler, "Velcro surfaces: Fast initialization of deformable models," *Comput. Vis. Image Understand.*, vol. 65, p. 237, 1997.
- [36] L. Zhukov, Z. Bao, I. Guskov, J. Wood, and D. Breen, "Dynamic deformable models for 3D MRI heart segmentation," presented at the SPIE Medical Imaging, San Diego, CA, 2002, unpublished.
- [37] G. Papandreou and P. Maragos, "Multigrid Geometric Active Contour Models," *IEEE Trans. Image Process.*, vol. 16, no. 1, pp. 229–240, Jun. 2007.
- [38] D. Geiger, A. Gupta, L. A. Costa, and J. Vlontzos, "Dynamic programming for detecting, tracking, and matching deformable contours," *IEEE Trans. Pattern Anal. Mach. Intell.*, vol. 17, no. 3, pp. 294–302, Mar. 1995.
- [39] J.-O. Lachaud and B. Taton, "Deformable model with a complexity independent from image resolution," *Computer Vision and Image Understanding*, vol. 99, pp. 453–475, 2005.
- [40] W. E. Lorensen and H. E. Cline, "Marching cubes: A high resolution 3D surface construction algorithm," *Comput. Graph.*, vol. 21, pp. 163–169, 1987.
- [41] D. Gordon and J. K. Udupa, "Fast surface tracking in three-dimensional binary images," *Comput. Vis., Graph., Image Process.*, vol. 45, pp. 196–214, 1989.
- [42] B. Li, A. V. Patil, J. A. Hossack, and S. T. Acton, "3D segmentation of the prostate via poisson inverse gradient initialization," presented at the IEEE Int. Conf. Image Processing, San Antonio, TX, 2007, unpublished.
- [43] C. Fox, *An Introduction to the Calculus of Variations*. New York: Dover, 1988.
- [44] R. Fattal, D. Lischinski, and M. Werman, "Gradient domain high dynamic range compression," *ACM Trans. Graph.*, vol. 21, pp. 249–256, 2002.
- [45] G. Arfken, *Mathematical Methods for Physicists*, 3rd ed. Orlando, FL: Academic, 1985.
- [46] P. Perez, M. Gangnet, and A. Blake, "Poisson image editing," *ACM Trans. Graph.*, vol. 22, pp. 313–318, 2003.
- [47] L. Giraud, R. Guivarch, and J. Stein, "Parallel distributed FFT-based solvers for 3-D poisson problems in meso-scale atmospheric simulations," *Int. J. High Performance Comput. Appl.*, vol. 15, pp. 36–46, 2001.
- [48] T. Matsumoto and T. Hanawa, "A fast algorithm for solving the poisson equation on a nested grid," *Astrophys. J.*, vol. 583, pp. 296–307, 2003.
- [49] M. S. Day, P. Colella, M. J. Lijewski, C. A. Rendleman, and D. L. Marcus, "Embedded boundary algorithms for solving the poisson equation on complex domains," *Lawrence Berkeley Nat. Lab.*, 1998, LBNL-41811.
- [50] Y. Saad, *Iterative Methods for Sparse Linear Systems*, 2nd ed. Philadelphia, PA: SIAM, 2003.
- [51] K. A. Atkinson, *An Introduction to Numerical Analysis*, 2nd ed. New York: Wiley, 1988.
- [52] L. P. Kobbelt, "Discrete fairing and variational subdivision for freeform surface design," *Vis. Comput.*, vol. 16, pp. 142–158, 2000.
- [53] G. Greiner, J. Loos, and W. Wesselink, "Data dependent thin plate energy and its use in interactive surface modeling," *Comput. Graph. Forum*, vol. 15, pp. 175–185, 1996.
- [54] Y. Yu and S. T. Acton, "Speckle reducing anisotropic diffusion," *IEEE Trans. Image Process.*, vol. 11, no. 11, pp. 1260–1270, Nov. 2002.
- [55] N. Ray, S. Acton, T. Altes, E. de Lange, and J. Brookeman, "Merging parametric active contours within homogeneous image regions for MRI based lung segmentation," *IEEE Trans. Med. Process.*, vol. 22, no. 2, Feb. 2003.
- [56] A. V. Patil, C. D. Garson, and J. A. Hossack, "3D Prostate elastography: Algorithm, simulations, and experiment," *Phys. Med. Biol.*, Dec. 2006.
- [57] S. A. Millington, B. Li, J. Tang, S. Trattig, J. R. Crandall, S. R. Hurwitz, and S. T. Acton, "Quantitative and topographical evaluation of ankle articular cartilage using high resolution MRI," *J. Orthopaed. Res.*, vol. 25, pp. 143–151, 2007.
- [58] D. Cohen-Steiner and J.-M. Morvan, "Second fundamental measure of geometric sets and local approximation of curvatures," *J. Diff. Geom.*, vol. 74, pp. 363–394, 2006.



Bing Li (S'06) received the B.S. degree in electrical and computer engineering from Peking (Beijing) University, Beijing, China, in 2003, and the M.S. and Ph.D. degrees in electrical engineering from the University of Virginia, Charlottesville, in 2005 and 2007, respectively.

He is working in the RAPID division for KLA-Tencor Corporation. His research interests include medical image analysis, image segmentation, active models, and target tracking.



Scott T. Acton (SM'99) graduated from Oakton High School, Vienna, Virginia, in 1984. He received the B.S. degree in electrical engineering from Virginia Tech, Blacksburg, in 1988, as a Virginia Scholar, and the M.S. and Ph.D. degrees in electrical and computer engineering from the University of Texas at Austin in 1990 and 1993, respectively, where he was a student of Prof. A. Bovik.

He has worked in industry for AT&T, Oakton, VA; the MITRE Corporation, McLean, VA; Motorola, Inc., Phoenix, AZ; and in academia for Oklahoma State University, Stillwater. Currently, he is Professor of electrical and computer engineering and biomedical engineering at the University of Virginia (UVA), Charlottesville. His research interests include anisotropic diffusion, basketball, active contours, biomedical segmentation problems, and biomedical tracking problems.

Dr. Acton is an active participant in the IEEE, currently serving as Associate Editor for the IEEE TRANSACTIONS ON IMAGE PROCESSING and, formerly, as Associate Editor for the IEEE SIGNAL PROCESSING LETTERS. He was the 2004 Technical Program Chair and the 2006 General Chair for the Asilomar Conference on Signals, Systems and Computers. At UVA, he was named the Outstanding New Teacher in 2002, Faculty Fellow in 2003, and Walter N. Munster Chair for Intelligence Enhancement in 2003.